Long Term X-Ray Spectral Variations of the Seyfert-1 Galaxy Mrk 279

K. Akhila[1] , Ranjeev Misra[2] , Savithri H. Ezhikode[3] , and K. Jeena[1]

[1] Department of Physics, Providence Women's College, University of Calicut, Kerala 673009, India; akhilasadanandan@gmail.com, jeenakarunakaran@gmail.com
[2] Inter-University Centre for Astronomy and Astrophysics (IUCAA), PB No.4, Ganeshkhind, Pune 411007, India
[3] Department of Physics and Electronics, CHRIST (Deemed to be University), Hosur Main Road, Bangalore 560029, India

Abstract

We present the results from a long term X-ray analysis of Mrk 279 during the period 2018–2020. We use data from multiple missions – AstroSat, NuSTAR and XMM-Newton, for the purpose. The X-ray spectrum can be modeled as a double Comptonization along with the presence of neutral Fe Kα line emission, at all epochs. We determined the source's X-ray flux and luminosity at these different epochs. We find significant variations in the source's flux state. We also investigate the variations in the source's spectral components during the observation period. We find that the photon index and hence the spectral shape follow the variations only over longer time periods. We probe the correlations between fluxes of different bands and their photon indices, and found no significant correlations between the parameters.

Key words: galaxies: Seyfert – galaxies: individual (Mrk 335) – X-rays: galaxies

1. Introduction

Seyfert-1 galaxies are the low-luminosity sub-class of active galaxies characterized by the presence of both broad and narrow emission lines in their spectra (e.g., Schmidt & Green 1983; Netzer 2015). The typical X-ray spectrum of a narrow line Seyfert 1 (NLS1) galaxy is a power law continuum with several features like the presence of broad and narrow emission lines and a smooth excess emission component at soft energies (Arnaud et al. 1985; Osterbrock & Pogge 1985; Boller et al. 1995; Fabian et al. 2000; Rani et al. 2019; Ezhikode et al. 2021; Mochizuki et al. 2023). The current understanding of the active galactic nucleus (AGN) structure tells us that these features arise from regions of varying environmental conditions, of significantly different temperatures and densities, around the central supermassive black hole.

All classes of AGNs are known to have variations in their X-ray fluxes. These variations occur over a wide range of timescales and amplitudes. AGN X-ray emission has been observed to exhibit variations of over a few ∼1000 s up to years with amplitude variations up to an order of magnitude (e.g., Turner et al. 1999). Studies have shown that the majority of NLS1 galaxies soften as they become brighter and that the variability is stronger in softer energies (Markowitz et al. 2003; Markowitz & Edelson 2004).

Markarian 279 (Mrk 279) is a nearby NLS1 galaxy at a redshift of $z = 0.0305$ (Scott et al. 2009) harboring a supermassive black hole of mass $M = 3.49 \times 10^7 M_\odot$ at its center (Peterson et al. 2004). It has been observed extensively in the X-ray energies by various missions. Early observations were made by HEAO 1 and Japan's ASCA mission (Dower et al. 1980; Weaver et al.

1995, 2001). Chandra, HST-STIS and FUSE observed the source simultaneously in 2002 May (Kaastra et al. 2004; Scott et al. 2004; Arav et al. 2005) and again in 2003 (Gabel et al. 2005; Arav et al. 2007; Costantini et al. 2007). Mrk 279 has also been observed multiple times by Chandra and XMM-Newton, independently (Yaqoob & Padmanabhan 2004; Jiang et al. 2019; Igo et al. 2020; Ursini et al. 2020). These observations have revealed that the X-ray flux of the source shows significant variations over time (Scott et al. 2004; Costantini et al. 2010; Ebrero et al. 2010).

Long term X-ray observations of Mrk 279 from 1979 to 1994 reveal a continuum flux variability going up to a factor of five, ranging between $1 - 5 \times 10^{-11}$ erg cm^{-2} s^{-1} (Weaver et al. 2001). Weaver et al. (2001) analyzed the ASCA observation from 1994 using a model consisting of two power laws and a narrow Gaussian. This showed that the 2–10 keV flux increased by 20% over the period of a few hours. In 2002, analysis of the Chandra observation using a continuum model consisting of two power laws modified by Galactic absorption found a low 2–10 keV flux of 1.2×10^{-11} erg cm^{-2} s^{-1} (Scott et al. 2004). Such low flux levels were previously observed in 1979 and 1991 (Weaver et al. 2001). The flux had dropped by a factor of two from a previous XMM-Newton observation in the same year. Scott et al. (2004) also reported the ultraviolet (UV) continuum flux to have decreased by a factor of ∼7.5 from 1999 to 2002. XMM-Newton acquired further observations of the source spread over multiple orbits during 2005 November. Costantini et al. (2010) found that at least three components are needed to give an acceptable description of the continuum spectrum. They fitted the epic-pn data using a broken power law and a modified blackbody

component. They calculated the 2–10 keV flux to be $\sim 2.5 \times 10^{-11}$ erg cm^{-2} s^{-1}. The Swift-BAT survey yielded a broadband flux of $\sim 3.8 \times 10^{-11}$ erg cm^{-2} s^{-1} in the 15–150 keV X-ray band (Cusumano et al. 2010).

Here, we use data from multiple missions to analyze the X-ray emissions from the source for a three year period extending from early 2018 to late 2020, so as to study its flux state and the variations that happen therein. This paper is structured as follows. The details of the observations used are given in Section 2. Section 3 discusses the processing techniques adopted for each data set. Spectral analysis is summarized in Section 4 and we analyze the flux variations of the source in Section 5. Finally the results are discussed in Section 6.

2. Observations

AstroSat, India's first multi-wavelength space observatory, enables simultaneous observations in the broad X-ray and UV bands. In this analysis, we use the first, and so far, the only, AstroSat observation of the source, made in 2018. We use the data from the Soft X-ray Telescope and Large Area X-ray Proportional Counter instruments on AstroSat (AstroSat: Agrawal 2006, SXT: Singh et al. 2017, LAXPC: Yadav et al. 2016; Agrawal et al. 2017; Antia et al. 2017; Misra et al. 2017). The NUclear Spectroscopic Telescope Array (NuS-TAR) has made observations of the source in the years 2019 and 2020. We chose the observation from 2019 and three orbits with enough exposure time in 2020 by the Focal Plane Modules (FPMA and FPMB) of NuSTAR (Harrison et al. 2010, 2013). Even though the NuSTAR observation from 2020 has been previously studied for multiple purposes (Akylas & Georgantopoulos 2021; Akylas et al. 2022; Kang & Wang 2022; Pal et al. 2023), our aim here is to analyze it for the variations in its X-ray flux state. We also use data from the epic-pn camera of the X-ray Multi-Mirror Mission (XMM-Newton: Jansen et al. 2001; Strüder et al. 2001) for this analysis. XMM-Newton has observed the source several times in the period 2002–2020; the earlier observations have been widely analyzed, as already discussed in Section 1. We selected the latest XMM-Newton observation with a 30.5 ks long exposure from 2020, the analysis of which has not been reported before. The details of all chosen data sets are summarized in Table 1.

3. Data Reduction

3.1. AstroSat

The SXT and LAXPC instruments on AstroSat observe X-ray sources in the 0.3–8.0 keV and 3.0–80.0 keV energy bands, respectively. SXT observations were made in the Photon Counting (PC) mode of the telescope. Level-1 data from 20 orbits of AstroSat-SXT were processed using the

Table 1
Observation Log Detailing the Date of Observation, Satellite, Mission id and Exposure Time

Mission	Observation Id	Date of Observation	Exposure Time (ks)
AstroSat SXT, LAXPC	9000001886	06-Feb-2018	39.94, 101
NuSTAR FPMA, FPMB	60160562002	29-Oct-2019	27.27
	60601011002	03-Aug-2020	62.02
	60601011004	05-Aug-2020	200.63
	60601011006	11-Aug-2020	52.80
XMM-Newton epic-pn	0872391301	20-Dec-2020	20.02

SXTPIPELINE 1.4B software and level-2 data were extracted. Data corresponding to all 20 orbits were then merged into a single cleaned event file. For this the event merger tool, SXTEVTMERGER, was used. The XSELECT task of HeaSoft was applied for filtering the data. A circular region of radius 15′ was chosen around the source and the spectrum was extracted. Blank sky background was used for the background spectrum. Response files (ARF and RMF) for the PC mode of the telescope, provided by the SXT-POC team, were used during spectral fitting.

LAXPC is a cluster of three identical proportional counters performing X-ray observations in a fairly broad energy band. We use data from LAXPC20 alone for our analysis as it has more stability in its response. The data were processed using LAXPCSOFT. The software's tools were employed to extract level-2 data, from which a fits event file was created. A filter file containing the good time intervals was also generated. The source and blank sky background spectra and the response files were extracted using the LAXPCSoftware.

3.2. NuSTAR

NuSTAR is an X-ray observatory operating in the 3–79 keV energy range. We use data from both the telescopes, FPMA and FPMB, for our analysis. NuSTAR Data Analysis Software NUSTARDAS_V2.1.1 package was utilized for processing the data. The NUPIPELINE was run using the latest calibration (CALDB) files. Output files were created and these were calibrated and cleaned using the created gti files. A circular region of size 38" was selected around the source and another region of similar size was selected for background extraction. Then the NUPRODUCTS task was run to extract spectral files and lightcurves. Science products were extracted for data from both the telescopes.
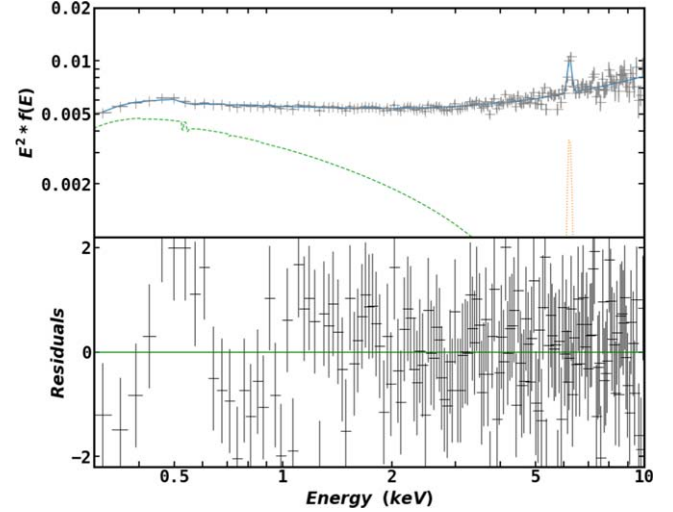
3.3. XMM-Newton

XMM-Newton is an X-ray observatory which makes observations in the 0.1–12 keV energy band. We use the data

from the epic-pn camera taken in imaging mode for our analysis. The Science Analysis Software SAS-20.0.0 was utilized for processing the data. We first created a raw event file using the EPCHAIN task and filtered the event file to remove flaring backgrounds. Then a gti file was created using TABGTIGEN. Only those data satisfying the conditions PATTERN ⩽4 and FLAG==0 were selected. SAS task EPATPLOT was applied to verify that the observation was free from any pile-up effect. We selected a circular region, centered around the source, with a radius of 40" and the spectrum was extracted. Similarly, background spectra were extracted from regions of the same size nearby, but excluding the source. Response files were generated using the tasks ARFGEN and RMFGEN.

4. Spectral Analysis

Spectral fitting was done using the χ^2 statistic. The spectral files were grouped so as to have a minimum of 30 counts in each bin. As advised by the LAXPC team, its spectrum was grouped at a 5% level, giving three energy bins per resolution. We use HeaSoft's spectral fitting package, XSPEC-12.12. (Arnaud 1996). The errors on the model parameters, obtained from XSPEC, give their 90% confidence interval. We fit the spectrum using two Comptonization components and a Gaussian component for the iron K-α emission line. Such a two corona model is widely used in literature to describe the observed X-ray spectrum of several NLS1 galaxies (Magdziarz et al. 1998; Czerny et al. 2003; Done et al. 2012; Petrucci et al. 2018; García et al. 2019). In this, the primary hard X-ray continuum is modeled to arise from the hot corona, explained as a power law emission due to a Comptonization component. In addition, there is another thermal Comptonization of seed photons from the far-UV end of accretion disk giving rise to the soft excess component. This is produced from a warm, optically thick layer of gas above the surface of the accretion disk and is distinct from the hot corona.

We use the diskbb model of XSPEC for the blackbody continuum from the accretion disk and this is convolved by thComp model of XSPEC. thComp, a convolution model which can be used for any seed photon distribution, is a replacement for the older nthComp model and agrees better with the Monte Carlo results for thermal Comptonization (Zdziarski et al. 2020). A fraction of the photons thus Comptonized are further upscattered by another Comptonization medium represented by the XSPEC model simpl (Steiner et al. 2009). simpl is again a simple convolution model that employs just two parameters to model Compton scattering, which makes it appropriate to be used in situations when the temperature of the corona is high and cannot be constrained by the data being fit. The Galactic absorption is modeled using the TBabs model of XSPEC with the absorption column density fixed to the value, $N_H = 1.78 \times 10^{20}$ cm^{-2} (Williams et al. 2006). We added the XSPEC model ztbabs to model the intrinsic absorption of the

Figure 1. XMM-Newton spectrum for the energy range 0.3–10.0 keV fit using theoretical model. Bottom panel shows the residuals of fit.

source. We found that this does not improve the fit and using more complicated models did not seem warranted and hence this component was not used in further analysis. Redshift of the source is fixed at z = 0.0304. Assuming a typical inner radius of ∼10R_g for the accretion disk of an NLS1 galaxy with a black hole mass $3.49 \times 10^7 M_\odot$ (Peterson et al. 2004), we fix the normalization of the diskbb component to the value 5.90×10^9. Here we consider the source to be at a distance of 124.1 Mpc (Pogge & Martini 2002) with an inclination angle of 30° (Weaver et al. 2001). Covering fraction of thComp is kept at unity so that all the seed photons from the disk undergo Compton upscattering.

We fit the 0.3–10.0 keV XMM-Newton spectrum observed in 2020 December using this model. The spectrum is plotted in Figure 1 and the best fit values of the parameters are listed in Table 2.

In order to probe the variations in corona over the years, we first fix the accretion disk as modeled by XMM-Newton data. Accordingly the inner disk temperature (T_{in}) is kept fixed at 4.8×10^{-3} keV. We also keep the optical depth of the warm corona (τ) and Gaussian line energy (E_l) fixed at 15.02 and 6.41 keV, respectively. We then use this model to fit AstroSat's combined SXT-LAXPC spectrum and the NuSTAR spectra. AstroSat SXT and LAXPC spectra are in the energy ranges 0.3–6.0 keV and 4.0–20.0 keV, respectively while NuSTAR covers a broad energy range of 3.0–79.0 keV. For the AstroSat spectrum, we added the constant model of XSPEC to accommodate the cross normalization between SXT and LAXPC20.

The free parameters of fit for AstroSat and NuSTAR data sets are listed in Table 3. We find that the photon index for the hot corona (Γsimpl) undergoes considerable changes during the period of observation. AstroSat data give a slightly higher
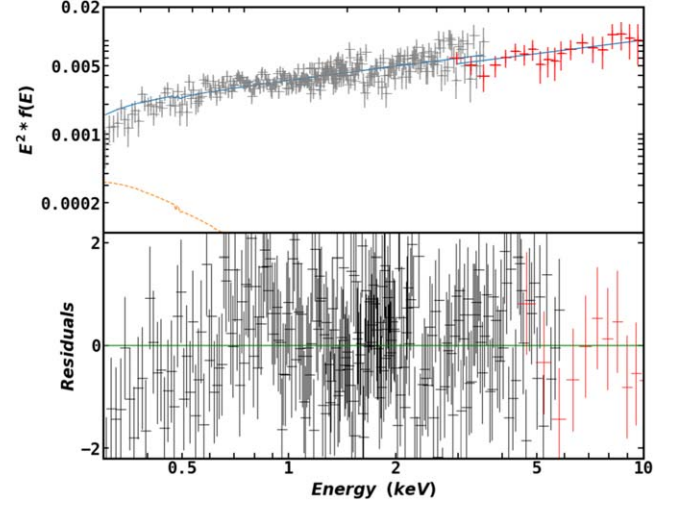
Table 2
XMM-Newton Spectral Fitting Parameters for the Broadband 0.3–10.0 keV Spectrum

Model Component	Parameter Value	XMM-Newton 0872391301
simpl	$\Gamma_{\rm simpl}$	$1.48^{+0.16}_{-0.21}$
	$f_{\rm Scat}(\times 10^{-2})$	$0.72^{+0.61}_{-0.39}$
thComp	τ	$15.02^{+2.38}_{-10.66}$
	kT_e (keV)	$0.98^{+2.09}_{-0.34}$
diskbb	$T_{\rm in}(\times 10^{-2}\,{\rm keV})$	$0.48^{+0.02}_{-0.03}$
zgauss	E_l (keV)	$6.41^{+0.04}_{-0.04}$
	σ (keV)	<0.14
	$N_{\rm gauss}(\times 10^{-5})$	$1.98^{+0.57}_{-0.53}$
χ^2/dof		158.66/159

Figure 2. Combined SXT - LAXPC spectrum fit using the theoretical model. Bottom panel shows the residuals of fit.

value (∼1.62) compared to XMM-Newton. Analyzing the NuSTAR data, we notice that the index increases to ∼1.8 for the observation from 2019 but then drops to ∼1.6 for the three observations in August 2020. We find that the scattering fraction also follows a similar pattern. We were also able to constrain the warm coronal temperature (kT_e) with an upper bound for all data sets. The AstroSat spectrum is not able to properly resolve the Gaussian line, nevertheless we obtained an upper constraint on its strength. The combined AstroSat spectrum is plotted in Figure 2 while Figure 3 plots all the NuSTAR spectra.

5. Variations in Coronal X-Ray Emission

From the spectra, we calculated the source's flux and hence luminosity in the 0.001–100.0 keV energy range at all the different epochs. This is tabulated in Table 4. We find that the source goes through large variations in its continuum flux over the three year timescale. The source flux increases by more than 50% from 2018 February to 2019 October. It then falls into a state of very low flux, with the flux values dropping by about 2 times. XMM-Newton observations from late 2020 show that the source has once again regained the flux, returning to its brighter state. Despite the changes in its flux states throughout the observation period, the source is constantly in a

brighter state, with the flux values being several times higher, compared to the earlier observations mentioned in Section 1. Recent insights into the cross calibration issue between NuSTAR and XMM-Newton epic suggest an empirical correction be added to the effective area (Fürst 2022; Kang & Wang 2023). We note that the epic fluxes being lower by about 20%, as mentioned by the XMM-Newton team, would not have a significant effect on the calculated flux for the current observation.

We then apply the cflux model of XSPEC to individual model components. Keeping the value of fractional scattering (f_{Scat}) fixed, we apply cflux to the entire Comptonization term, simpl*thComp*diskbb and then to thComp*diskbb alone. The former term gives the value of the flux we observe as being due to the two coronal components, the net continuum flux. It includes the flux of photons that underwent scattering by both coronae plus the flux from the remaining photons which were scattered by the warm corona alone. We call this flux the net continuum flux (NCM), since it does not include the line emission. The latter term gives the total flux upscattered from

Table 3
Spectral Parameter Values for the AstroSat and NuSTAR Observations

Model Component	Parameter Value	AstroSat 9000001886	NuSTAR 60160562002	60601011002	60601011004	60601011006
simpl	$\Gamma_{\rm simpl}$	$1.62^{+0.04}_{-0.04}$	$1.83^{+0.04}_{-0.04}$	$1.63^{+0.02}_{-0.02}$	$1.62^{+0.01}_{-0.01}$	$1.59^{+0.04}_{-0.05}$
	$f_{\rm Scat}(\times 10^{-2})$	$1.46^{+0.37}_{-0.30}$	$5.83^{+3.69}_{-1.39}$	$0.76^{+0.06}_{-0.19}$	$0.70^{+0.39}_{-0.15}$	$0.70^{+0.26}_{-0.18}$
thcomp	kT_e (keV)	<0.52	<1.02	<0.81	<0.77	$0.83^{+0.07}_{-0.25}$
zgauss	σ (keV)	0.08(frozen)	$0.24^{+0.1}_{-0.1}$	<0.23	$0.27^{+0.07}_{-0.06}$	$0.36^{+0.39}_{-0.21}$
	$N_{\rm Gauss}\,(\times 10^{-5})$	<3.20	$5.62^{+1.54}_{-1.42}$	$1.95^{+0.49}_{-0.45}$	$2.33^{+0.38}_{-0.29}$	$1.96^{+1.28}_{-0.79}$
χ^2/dof		271.96/270	502.32/509	373.98/396	762.99/740	379.15/403
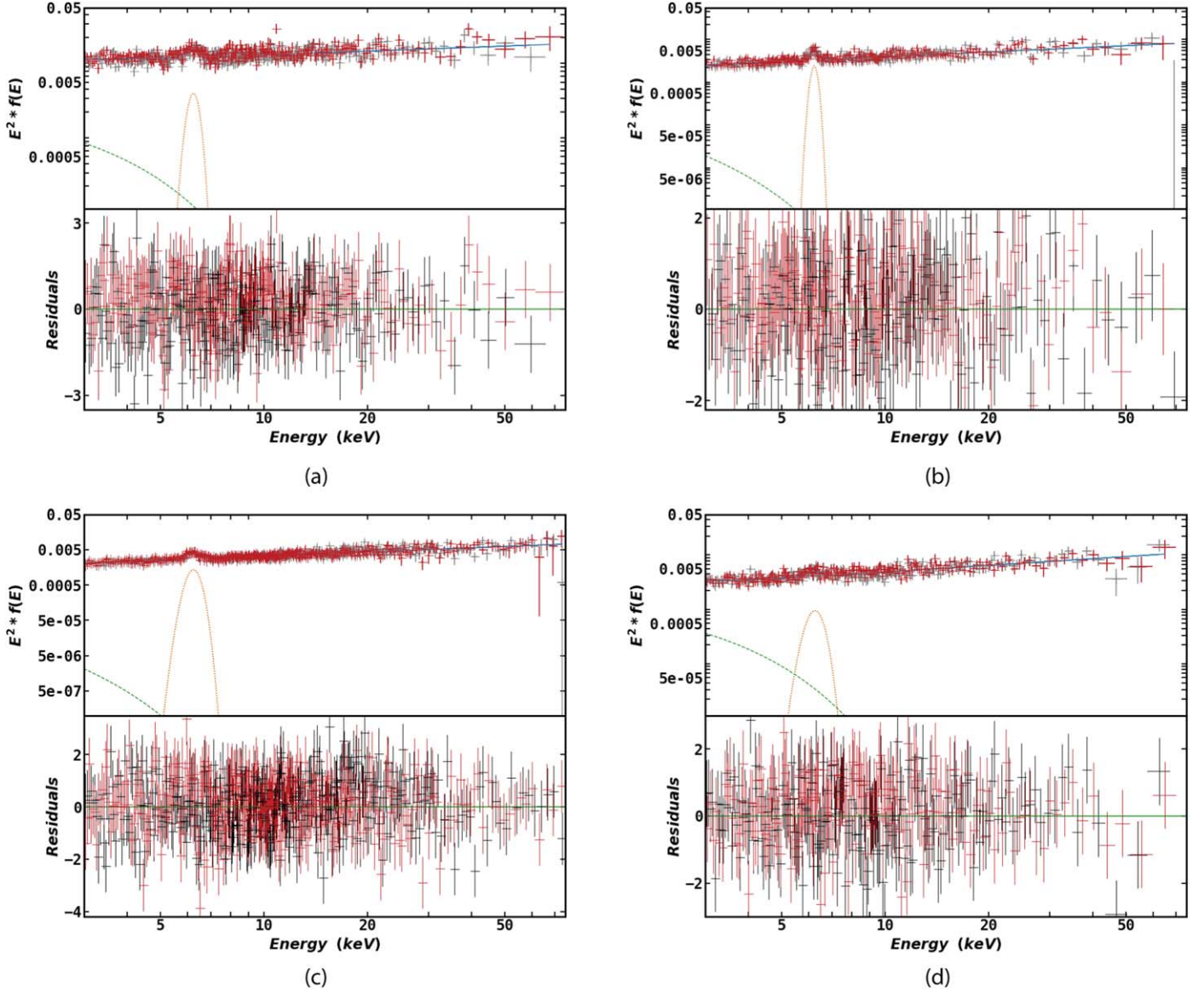
Figure 3. The NuSTAR 3.0–79.0 keV spectra fit using the theoretical model. Top panels shows the unfolded spectrum along with the model while bottom panel plots the residuals of fit. Starting from the top left corner, the different figures correspond to the (a) 60160562002, (b) 60601011002, (c) 60601011004 and (d) 60601011006 NuSTAR observations, respectively.

the warm corona. It would have been observed as being the result of upscattering by the warm corona, had the hot corona not been present and is indicative of the properties of the warm coronal component (WCM: cflux*thcomp*diskbb). Both terms include the flux from the disk component. This is estimated by applying cflux to diskbb alone. The flux obtained from the accretion disk is 6.46×10^{-11} erg cm^{-2} s^{-1}. Applying cflux to the Gaussian component (zgauss), with the normalization (N_{Gauss}) fixed, gives the emission line flux. This Gaussian line corresponding to iron Kα emission contributes very little to the overall flux, with its strength being roughly around $\sim$2 orders less than the Comptonization fluxes. The AstroSat observation

from 2018 is not able to resolve this emission line properly. However we were able to constrain its strength and it agrees well with the observations from the other epochs, within the 90% confidence interval. In accordance with the low values of the emission line flux, a major contribution to the total flux comes from the Comptonization component. This is seen in Figure 4 where the individual spectral components are plotted, showing their variations during the observation period. We find that the model components closely follow the pattern of the total flux, rising, falling and then returning back to the original state over the three year timescale. All the flux values are tabulated in Table 5.
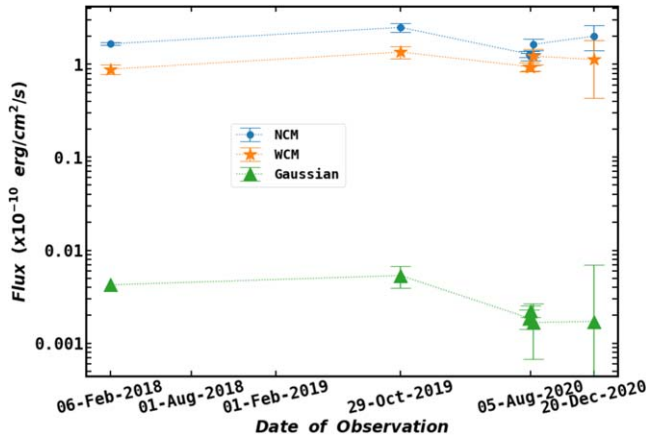
Table 4
Broadband X-Ray Flux and Luminosity of Mrk 279, Calculated in the Energy Range 0.001–100.0 keV, Over the Years from 2018 to 2020

Date of Observation	Mission	Flux ($\times 10^{-11}$ erg cm^{-2} s^{-1})	Luminosity ($\times 10^{44}$ erg s^{-1})
06-Feb-2018	AstroSat	$16.61_{\pm 0.54}$	$3.06_{\pm 0.10}$
29-Oct-2019	NuSTAR	$25.00_{\pm 2.64}$	$4.61_{\pm 0.49}$
03-Aug-2020	NuSTAR	$13.19_{\pm 1.34}$	$2.43_{\pm 0.25}$
05-Aug-2020	NuSTAR	$12.05_{\pm 0.92}$	$2.22_{\pm 0.17}$
11-Aug-2020	NuSTAR	$16.44_{\pm 2.36}$	$3.03_{\pm 0.43}$
20-Dec-2020	XMM-Newton	$19.75_{\pm 6.45}$	$3.64_{\pm 1.19}$

Table 5
The Net Continuum Flux (NCM), Warm Corona Flux (WCM) and the Emission Line (Gaussian) Flux for Mrk 279 Through the Three Year Timescale

Date of Observation	Mission	NCM ($\times 10^{-11}$)	WCM ($\times 10^{-11}$)	Gaussian ($\times 10^{-13}$)
06-Feb-2018	AstroSat	$16.61_{\pm 0.54}$	$8.87_{\pm 0.99}$	<4.26
29-Oct-2019	NuSTAR	$24.96_{\pm 2.65}$	$13.57_{\pm 2.10}$	$5.37_{\pm 1.43}$
03-Aug-2020	NuSTAR	$12.85_{\pm 1.01}$	$9.42_{\pm 1.01}$	$1.86_{\pm 0.45}$
05-Aug-2020	NuSTAR	$12.02_{\pm 1.06}$	$9.18_{\pm 0.63}$	$2.23_{\pm 0.33}$
11-Aug-2020	NuSTAR	$16.42_{\pm 2.36}$	$12.25_{\pm 2.35}$	$1.67_{\pm 1.00}$
20-Dec-2020	XMM-Newton	$20.06_{\pm 6.06}$	$11.27_{\pm 6.92}$	$1.71_{\pm 5.31}$

Figure 5. The fraction of warm Comptonized flux (WCM) to the total flux, showing its variations over the time period from 2018 to 2020.
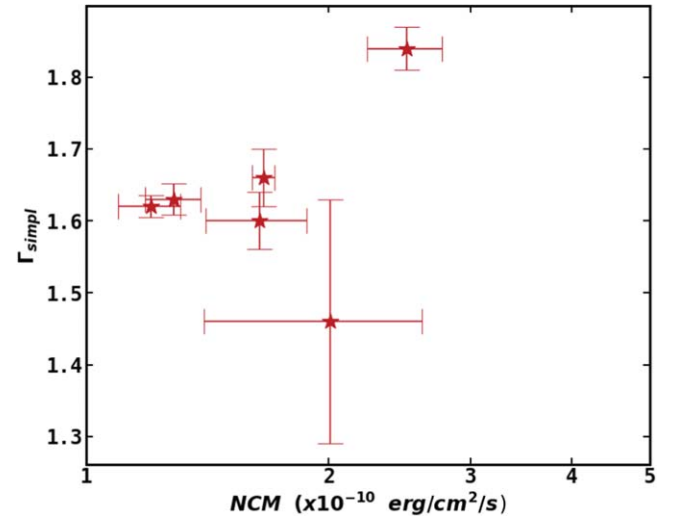
Figure 6. Hot photon index (Γ_{simpl}) plotted against the net continuum flux (NCM). The data do not seem to exhibit any significant correlation between the parameters; the Pearson correlation coefficient obtained was 0.41 with a two-sided p-value of 0.42.

Figure 4. X-ray flux variations of Mrk 279 during the period from 2018–2020. The net continuum flux (NCM), warm corona flux (WCM) and emission line flux (Gaussian) are plotted in colors blue, orange and green, respectively.

Akin to the strength of the emission line, we were unable to constrain the Gaussian width (σ) from the AstroSat spectrum. However, analysis with NuSTAR and XMM-Newton reveals a sudden change in the line width. NuSTAR data from 2019 and August 2020 exhibit a broad iron line of width in the range 0.2–0.3 keV. But in December 2020, an XMM-Newton spectrum disclosed a swift reduction in its value, where we constrain it with an upper bound of 0.14 keV.

6. Summary and Discussion

In this work, we look at the X-ray spectrum of Mrk 279 over a period of three years to study the variations in its flux state. We also study the fluxes from the different spectral components in the spectrum and analyze their long term variations. We find that the flux values of all the spectral components of the source change considerably during this period, as is evident from

Figure 4, while in Figure 5 we plot the fraction of the warm Comptonized flux (WCM) to the total flux.

Unlike the spectral flux, the shape of the spectrum does not exhibit short term variations (the photon index remains at ~1.6 for all NuSTAR observations from 2020 August). Over longer periods of time, the spectral photon index seems to follow the trend of the continuum flux at all epochs, except in 2020 December where the flux regains its previous high state but the index drops down further.

Correlation between the continuum flux and photon index has been the subject of several previous studies (e.g., Singh et al. 1991; Yaqoob & Warwick 1991; Dewangan et al. 2002; Grupe et al. 2012; Barua et al. 2020). Such a correlation could arise if the X-ray variability is due to the change in the seed photon population; in this case the physical property of the corona may vary with the flux. Another possibility in the two component scenario is of a superposition of soft, variable power law associated with coronal emission and another harder spectral component with much less variability (see: Shih et al. 2002; Fabian & Vaughan 2003; Markowitz et al. 2003). Nevertheless we found no significant correlation between the parameters; we obtained a Pearson correlation coefficient of 0.41 between the photon index (Γ_{simpl}) and the net continuum flux, with a two sided p-value of 0.42. Figure 6 shows the plot of Γ_{simpl} versus the flux.

In conclusion, we find that, in agreement with the previous studies, Mrk 279 shows significant variations in its flux state and hence, its luminosity. This pattern is closely followed by the spectral components as well. We also notice that the photon index and hence the spectral shape follow the flux variations over longer periods of time. However, neither the index or the spectral shape is seen to exhibit the short term changes seen in the X-ray flux. Subsequently, we plan to include UV data from AstroSat's UVIT mission to obtain a broadband spectral model and analyze the correlations between variabilities in the different energy bands.

ORCID iDs

K. Akhila ● https://orcid.org/0009-0004-9776-904X
Ranjeev Misra ● https://orcid.org/0000-0002-7609-2779
Savithri H. Ezhikode ● https://orcid.org/0000-0003-1795-3281

References

Agrawal, P. 2006, AdSpR, 38, 2989
Agrawal, P., Yadav, J., Antia, H., et al. 2017, JApA, 38, 1
Akylas, A., & Georgantopoulos, I. 2021, A&A, 655, A60
Akylas, A., Papadakis, I., & Georgakakis, A. 2022, A&A, 666, A127
Antia, H., Yadav, J., Agrawal, P., et al. 2017, ApJS, 231, 10
Arav, N., Gabel, J. R., Korista, K. T., et al. 2007, ApJ, 658, 829
Arav, N., Kaastra, J., Kriss, G. A., et al. 2005, ApJ, 620, 665
Arnaud, K. 1996, ASPC, 101, 17
Arnaud, K., Branduardi-Raymont, G., Culhane, J., et al. 1985, MNRAS, 217, 105
Barua, S., Jithesh, V., Misra, R., et al. 2020, MNRAS, 492, 3041
Boller, T., Brandt, W. N., & Fink, H. 1995, arXiv:astro-ph/9504093
Costantini, E., Kaastra, J., Korista, K., et al. 2010, A&A, 512, A25
Costantini, E., Kaastra, J. S., Arav, N., et al. 2007, A&A, 461, 121
Cusumano, G., La Parola, V., Segreto, A., et al. 2010, A&A, 524, A64
Czerny, B., Nikołajuk, M., Różańska, A., et al. 2003, A&A, 412, 317
Dewangan, G., Boller, T., Singh, K., & Leighly, K. 2002, A&A, 390, 65
Done, C., Davis, S., Jin, C., Blaes, O., & Ward, M. 2012, MNRAS, 420, 1848
Dower, R., Bradt, H., Doxsey, R., Johnston, M., & Griffiths, R. 1980, ApJ, 235, 355
Ebrero, J., Costantini, E., Kaastra, J., et al. 2010, A&A, 520, A36
Ezhikode, S. H., Dewangan, G. C., & Misra, R. 2021, JApA, 42, 51
Fabian, A., Iwasawa, K., Reynolds, C., & Young, A. 2000, PASP, 112, 1145
Fabian, A., & Vaughan, S. 2003, MNRAS, 340, L28
Fürst, F. 2022, XMM-Newton Calibration Technical Note XMM-SOC-CAL-TN-0230, European Space Agency
Gabel, J. R., Arav, N., Kaastra, J. S., et al. 2005, ApJ, 623, 85
García, J. A., Kara, E., Walton, D., et al. 2019, ApJ, 871, 88
Grupe, D., Komossa, S., Gallo, L. C., et al. 2012, ApJS, 199, 28
Harrison, F. A., Boggs, S., Christensen, F., et al. 2010, Proc. SPIE, 7732, 189
Harrison, F. A., Craig, W. W., Christensen, F. E., et al. 2013, ApJ, 770, 103
Igo, Z., Parker, M., Matzeu, G., et al. 2020, MNRAS, 493, 1088
Jansen, F., Lumb, D., Altieri, B., et al. 2001, A&A, 365, L1
Jiang, J., Fabian, A. C., Dauser, T., et al. 2019, MNRAS, 489, 3436
Kaastra, J., Raassen, A., Mewe, R., et al. 2004, A&A, 428, 57
Kang, J.-L., & Wang, J.-X. 2022, ApJ, 929, 141
Kang, J.-L., & Wang, J.-X. 2023, arXiv:2311.15499
Magdziarz, P., Blaes, O. M., Zdziarski, A. A., Johnson, W. N., & Smith, D. A. 1998, MNRAS, 301, 179
Markowitz, A., & Edelson, R. 2004, ApJ, 617, 939
Markowitz, A., Edelson, R., & Vaughan, S. 2003, ApJ, 598, 935
Misra, R., Yadav, J., Chauhan, J. V., et al. 2017, Astrophys. J., 835, 195
Mochizuki, Y., Mizumoto, M., & Ebisawa, K. 2023, MNRAS, 525, 922

Netzer, H. 2015, ARA&A, 53, 365
Osterbrock, D. E., & Pogge, R. W. 1985, ApJ, 297, 166
Pal, I., Sreehari, H., Rameshan, G., et al. 2023, arXiv:2310.18196
Peterson, B. M., Ferrarese, L., Gilbert, K., et al. 2004, ApJ, 613, 682
Petrucci, P.-O., Ursini, F., De Rosa, A., et al. 2018, A&A, 611, A59
Pogge, R. W., & Martini, P. 2002, ApJ, 569, 624
Rani, P., Stalin, C., & Goswami, K. 2019, MNRAS, 484, 5113
Schmidt, M., & Green, R. F. 1983, ApJ, 269, 352
Scott, J. E., Arav, N., Gabel, J. R., et al. 2009, ApJ, 694, 438
Scott, J. E., Kriss, G. A., Lee, J. C., et al. 2004, ApJS, 152, 1
Shih, D., Iwasawa, K., & Fabian, A. 2002, MNRAS, 333, 687
Singh, K., Rao, A., & Vahia, M. 1991, A&A, 248, 37
Singh, K., Stewart, G., Westergaard, N., et al. 2017, JApA, 38, 29

Steiner, J. F., Narayan, R., McClintock, J. E., & Ebisawa, K. 2009, PASP, 121, 1279
Strüder, L., Briel, U., Dennerl, K., et al. 2001, A&A, 365, L18
Turner, T., George, I., Nandra, K., & Turcan, D. 1999, ApJ, 524, 667
Ursini, F., Dovčiak, M., Zhang, W., et al. 2020, A&A, 644, A132
Weaver, K., Arnaud, K., & Mushotzky, R. 1995, ApJ, 447, 121
Weaver, K., Gelbord, J., & Yaqoob, T. 2001, ApJ, 550, 261
Williams, R. J., Mathur, S., & Nicastro, F. 2006, ApJ, 645, 179
Yadav, J., Agrawal, P., Antia, H., et al. 2016, Proc. SPIE, 9905, 374
Yaqoob, T., & Padmanabhan, U. 2004, ApJ, 604, 63
Yaqoob, T., & Warwick, R. 1991, MNRAS, 248, 773
Zdziarski, A. A., Szanecki, M., Poutanen, J., Gierliński, M., & Biernacki, P. 2020, MNRAS, 492, 5234